

RESEARCH ARTICLE

10.1002/2016WR018678

Key Points:

- Scenarios of bentonite buffer wetting in low-permeability fractured rock are explored by numerical modeling
- Results are compared to values obtained in a field experiment at the AAspoe Hard Rock laboratory
- Inflow heterogeneity influences more the bentonite wetting than the total open-hole inflow rate

Supporting Information:

- Supporting Information S1
- Movie S1
- Movie S2

Correspondence to:

B. Dessirier,
benoit.dessirier@natgeo.su.se

Citation:

Dessirier, B., A. Frampton, Å. Fransson, and J. Jarsjö (2016), Modeling early in situ wetting of a compacted bentonite buffer installed in low permeable crystalline bedrock, *Water Resour. Res.*, 52, 6207–6221, doi:10.1002/2016WR018678.

Received 25 JAN 2016

Accepted 23 JUL 2016

Accepted article online 29 JUL 2016

Published online 12 AUG 2016

Modeling early in situ wetting of a compacted bentonite buffer installed in low permeable crystalline bedrock

B. Dessirier¹, A. Frampton¹, Å. Fransson², and J. Jarsjö¹

¹Department of Physical Geography, Stockholm University, Stockholm, Sweden, ²Division of GeoEngineering, Chalmers University of Technology, Gothenburg, Sweden

Abstract The repository concept for geological disposal of spent nuclear fuel in Sweden and Finland is planned to be constructed in sparsely fractured crystalline bedrock and with an engineered bentonite buffer to embed the waste canisters. An important stage in such a deep repository is the postclosure phase following the deposition and the backfilling operations when the initially unsaturated buffer material gets hydrated by the groundwater delivered by the natural bedrock. We use numerical simulations to interpret observations on buffer wetting gathered during an in situ campaign, the Bentonite Rock Interaction Experiment, in which unsaturated bentonite columns were introduced into deposition holes in the floor of a 417 m deep tunnel at the Äspö Hard Rock Laboratory in Sweden. Our objectives are to assess the performance of state-of-the-art flow models in reproducing the buffer wetting process and to investigate to which extent dependable predictions of buffer wetting times and saturation patterns can be made based on information collected prior to buffer insertion. This would be important for preventing insertion into unsuitable bedrock environments. Field data and modeling results indicate the development of a de-saturated zone in the rock and show that in most cases, the presence or absence of fractures and flow heterogeneity are more important factors for correct wetting predictions than the total inflow. For instance, for an equal open-hole inflow value, homogeneous inflow yields much more rapid buffer wetting than cases where fractures are represented explicitly thus creating heterogeneous inflow distributions.

1. Introduction and Background

Geological disposal concepts for long-lived radioactive waste such as spent nuclear fuel are generally based on adopting multibarrier methods [Krauskopf, 1988; Pusch, 2009], since different protective barriers can serve to reduce an overall risk of leakage of radionuclides from the repository to the biosphere. A design concept under development in Sweden and Finland, denoted as the KBS-3 method, consists in excavating deposition tunnels at approximately 500 m below ground level in sparsely fractured and low permeable crystalline bedrock [Johannesson *et al.*, 2007]. Spent nuclear fuel assemblies are then to be placed in iron inserts inside sealed copper canisters which in turn are placed in deposition holes, embedded in a buffer material composed of bentonite clay. Thereafter, upon closure of the deposition tunnel, these will also be backfilled using a bentonite-based material [Pusch, 2009; SKB, 2010]. The design concept distinguishes between the *engineered barrier system* and the *natural barrier system*, the latter consisting of the geologic formation, i.e., the host bedrock in which the repository is constructed.

Crystalline rock environments are generally considered favorable host systems [National Research Council, 1996] since they are typically sparsely fractured and have very low permeability combined with strong material retention properties [Neretnieks, 1980; Moreno and Neretnieks, 1993; Cvetkovic *et al.*, 1999, 2004]. Models of sparsely fractured rock generally involve describing flow and transport pathways through fractures [Dverstorp *et al.*, 1992; Niemi *et al.*, 2000; Huseby *et al.*, 2001; Follin *et al.*, 2008; Frampton and Cvetkovic, 2010, 2011], which can readily be combined with tracer retention processes such as matrix diffusion and sorption [Cvetkovic and Frampton, 2010, 2012] as well as radionuclide decay chains [Selroos and Painter, 2012]. Hydrogeological flow models then typically consider flow through fractures only, or treat rock matrix permeability as isotropic and homogeneous, which may represent unrealistic model simplification [Neuman, 2005; Fiori *et al.*, 2010], although notable exceptions exist [Blessent *et al.*, 2011].

The bentonite buffer is a part of the engineered barrier system, and is designed to swell and seal potential gaps left during construction and to have a strong chemical adsorption capacity [Pusch, 2009]. Thereby the bentonite buffer acts as a critical interface to the host geological formation and bedrock. The bentonite buffer is planned to be inserted with a predetermined initial water content and dry density, which will depend on the target swelling pressure that should be reached at full saturation [Alonso *et al.*, 2005]. An initially unsaturated buffer means that two-phase (gas and liquid) flow will occur for air and water immediately after the installation of the buffer and for some time thereafter. This is primarily expected to happen while the installed bentonite buffer re-saturates, as formation water flows toward the regions consisting of buffer and backfill material. The near rock mass may also become de-saturated by prolonged exposure to atmospheric conditions [Finsterle and Pruess, 1995] prior to buffer insertion, potential groundwater degassing [Jarsjö and Destouni, 2000] or because the high water suction of subsequently inserted unsaturated bentonite locally induces a de-saturation of the surrounding rock [Gens *et al.*, 2002; Dessirier *et al.*, 2014]. Groundwater and air flow patterns near the interface between the engineered and the natural barriers are subject to even more complexity due to the extreme heterogeneity of fractured crystalline rock.

In order to ensure that imposed safety standards for deep repositories are met, criteria need to be formulated regarding buffer properties and host rock properties, not least considering potential physical and geochemical heterogeneities, which may govern transport pathways from the canister environment to the biosphere. In particular, criteria on the suitability of deposition holes to host functioning buffers must be formulated such that they can be assessed based on empty holes prior to canister and buffer insertion. Tentative criteria are based on total deposition hole inflow before installation, where the main concern is to prevent piping and buffer erosion which can potentially occur for sufficiently fast and concentrated channel flows [Sandén and Börgesson, 2010]. However, the above-mentioned two-phase flow and buffer saturation processes may also have important implications for the functioning of the buffer. It may for instance be less preferable to have long (e.g., decadal or centennial) time periods of unsaturated conditions, during which air would be present as a separate phase influencing biogeochemical reactions, and during which swelling pressures would not be fully developed. A further question is then whether or not, or to which extent, deposition hole inflow characteristics prior to buffer installation can reflect subsequent saturation dynamics of the buffer.

The focus of this study is on key hydrogeological flow processes and effects occurring at and near the interface between the host geological rock formation and the engineered bentonite clay buffer. Specifically, we investigate relations between deposition hole inflow and subsequent transient wetting of the buffer under the two-phase flow regime in the vicinity of the deposition hole. To map and explore different sets of inflow conditions we will conceptually distinguish between the (total) inflow rate into the deposition hole, ranging from low to high, and the near-field permeability structure that governs the spatial inflow distribution over the deposition hole wall, ranging from a smooth homogeneous inflow to localized heterogeneous inflow. The specific questions we aim at answering in this paper are:

1. Can models calibrated to open-hole inflow values capture, quantitatively or qualitatively, the dynamic two-phase flow conditions that will prevail in the buffer and adjacent rock, after buffer installation?
2. To what extent can criteria on inflow rate and distribution inside a deposition hole prior to installation constrain wetting patterns and times of the installed buffer?

To answer these questions, the present paper will explore several realistic scenarios based on in situ field conditions using numerical modeling. The models are designed with the aim to reproduce a series of experiments, denoted as the Bentonite Rock Interaction Experiments (BRIE) [Fransson *et al.*, 2015, 2012; Holton *et al.*, 2012], which were carried out in a tunnel in the deep bedrock at the Äspö Hard Rock Laboratory (HRL) in Southeastern Sweden. BRIE allowed the observation of isothermal wetting of bentonite under in situ conditions. Thermal processes caused by heat generation from radioactive decay in actual canisters were not considered by this setup. Their influence was for example assessed in a more generic parametric study by Gens *et al.* [2002]. The first phase of the experiments consisted in characterizing the rock mass and fracture zones surrounding a tunnel situated at -417 m depth via five exploration boreholes. In the second phase, the characterization continued after additional boreholes were drilled surrounding the first five and two original boreholes were expanded into small-scale deposition holes of 30 cm in diameter and approximately 3 m height in the floor of the tunnel. The last phase consisted of the installation, monitoring and characterization after retrieval of bentonite packages after approximately one and a half years in each

deposition hole, while permeability and retention curve parameters were measured in the laboratory on previously collected rock matrix samples. In this paper, the experimental data serve as a basis in the development of a tunnel scale fractured rock model of the BRIE site, common for all the presented simulations. These observational data also assist in creating realistic deposition hole scale inflow scenarios, which honor the measured inflow values and/or fracture locations observed in each of the two BRIE deposition holes. Furthermore, predictive runs of bentonite wetting under the different scenarios are presented, compared against available field and experimental data, and discussed in the context of their usability as assessment criteria.

2. Tunnel Scale Model Development

The model domain adopted for this study is a $40 \times 40 \times 40$ m rock mass surrounding the “Y”-shaped end of a tunnel approximately 417 m below ground at the Äspö HRL (Figure 1a, see also supporting information, movies S1 and S2). This extent was selected to reach stable boundary conditions, considering also the position of neighboring tunnels and known deformation zones.

The flow solver used is based on a continuous representation of the geological media and on the integrated finite difference discretization for which cell volumes and cell connections need to be defined. This is done in a two-step process:

1. distributing cell centers with associated material tags in the modeling domain,
2. computing the Voronoi tessellation over the cell centers and exporting the cell volumes and connections to the format required by the flow solver.

This method allows refinement of the mesh around features of interest, e.g., deposition holes and fractures, by locally increasing the cell center density (step 1 above). To honor a specific cell boundary, one needs to anticipate the coming application of the Voronoi rule (step 2), which can become complex if several features intersect in a close proximity [Hyman *et al.*, 2014]. However, in the present case, the number of intersecting fractures explicitly accounted for and represented in the model is relatively small, making the complexity manageable.

Cell centers from an existing flow model for the Äspö HRL [Svensson *et al.*, 2008] were extracted and classified as open tunnel cells, tunnel wall cells, or bedrock cells. Open tunnel cells act as atmospheric boundary conditions. Tunnel wall cells consist of bedrock but are classified separately in order to consider material property changes representative of an excavation-damaged zone (EDZ) or to exhibit permeability reduction due to mechanical or two-phase flow effects. Background rock cells convey together the hydraulic behavior of intact rock blocks separated by fractures that are not explicitly accounted for. The cell center spacing is typically 1–2 m close to the tunnel and 2–4 m further away as can be seen in the resulting distribution of cell sizes, defined as the cubic root of the cell volume (Figure 1c).

The domain is intersected by three known fracture zones represented in Figure 1a: wfrac1 in blue with an estimated transmissivity $T = 4.0 \cdot 10^{-9} \text{ m}^2/\text{s}$, wfrac2 in green with $T = 2.0 \cdot 10^{-9} \text{ m}^2/\text{s}$ and NW4 in purple with $T = 6.5 \cdot 10^{-7} \text{ m}^2/\text{s}$. These are meshed by regularly spaced point sets later added to the list of cell centers. One additional class is introduced for tunnel wall cells that share a connection with explicit fracture zone cells. Inside the fracture plane the typical fracture element size is approximately 3 m (Figure 1a). The fracture zones are modeled with an effective width of 1 m and a permeability value consistent with the transmissivity values measured by hydraulic tests performed during BRIE.

The Voronoi tessellation is then computed using the voro++ library [Rycroft, 2009] to obtain all the necessary cell and connection information. A specific verification is made to ensure that explicit fracture elements are connected as expected and that the tunnel geometry has been reproduced accurately enough by tessellating the cell centers from the parent Äspö flow model [Svensson *et al.*, 2008]. For long-term tunnel inflow, which in this context is relevant for use as starting condition for the actual BRIE/two-phase flow simulations, the gas phase is expected to be continuously connected to the tunnel and the atmospheric boundary; hence, air entrapment effects can reasonably be neglected [Dessirier *et al.*, 2014]. We therefore used the flow solver TOUGH2 with equation of state 9 (EOS9) for saturated-unsaturated flow based on water mass balance [Pruess *et al.*, 1999], to obtain the relevant initial conditions for the transient BRIE simulations before the insertion of the bentonite buffer (section 3.2). For convergence, the relative tolerance criterion

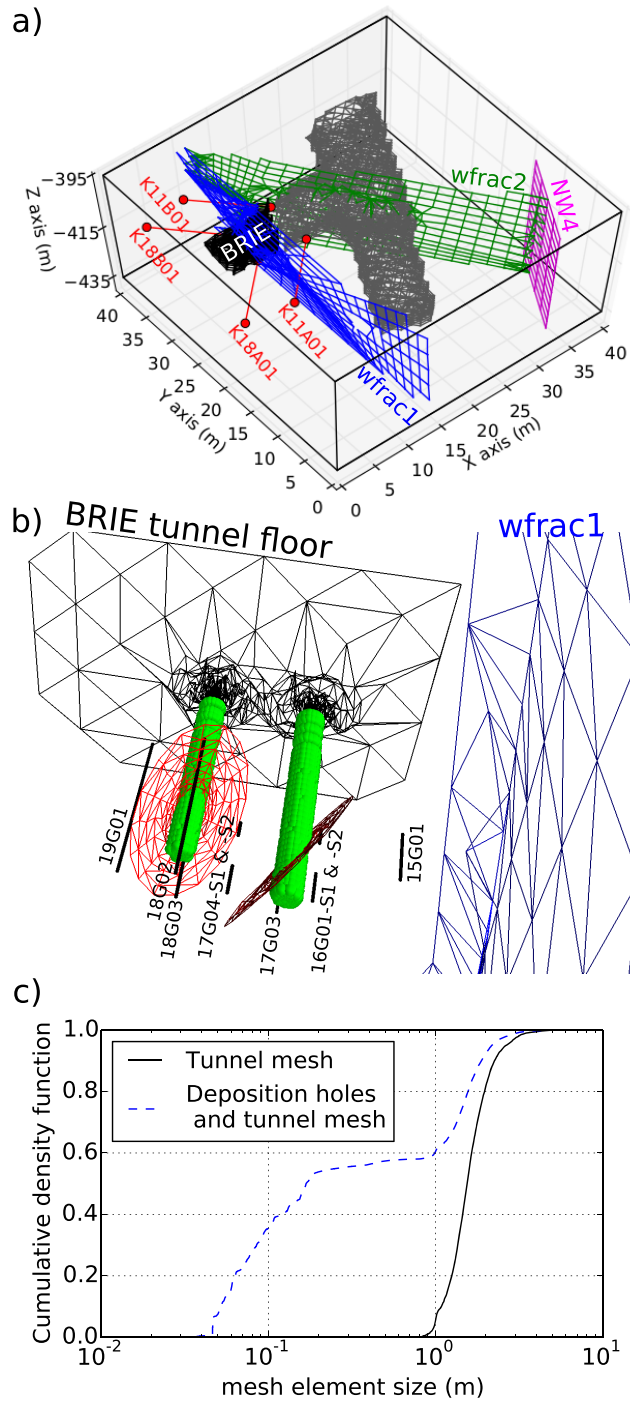


Figure 1. (a) Modeling domain (black) including the main tunnel (grey), the BRIE tunnel (black), the four long boreholes (red) and the major deformation zones: wfrac1 (blue), wfrac2 (green) and NW4 (purple). The major fractures zones considered in the model are illustrated by the mesh connections between fracture volumes, whereas for visual clarity, background rock cells are not shown. (b) Refined deposition hole mesh. The BRIE tunnel floor is shown in black in the background, wfrac1 in blue to the right, the deposition holes (left) 18 and (right) 17 in green, the local fractures in red, and the local probing borehole intervals in black and labeled. (c) Mesh element size distributions for the steady state tunnel model and the refined model with tunnel and deposition holes.

for maximum normalized residuals in the numerical solver is set to 10^{-5} which is the default value in TOUGH2. The python library PyTOUGH [Croucher, 2011] is used as a flexible scripted model setup and data management tool. Two constitutive relationships are needed for unsaturated conditions and defined based on the parameterization given by Van Genuchten [1980] and the scaling relationship proposed by Leverett [1941]:

$$k_l = k_{sat} \cdot \sqrt{S_l} (1 - [1 - (S_l)^{1/\lambda}]^\lambda)^2 \quad (1)$$

$$p_{cap} = -p_0(k_{sat}) \cdot (S_l^{-1/\lambda} - 1)^{1-\lambda} \quad (2)$$

$$p_0(k_{sat}) = p_{0,ref} \cdot \sqrt{\frac{k_{sat,ref}}{k_{sat}}} \quad (3)$$

with k_l the liquid phase permeability, k_{sat} the saturated permeability, S_l the effective liquid phase saturation, p_{cap} the capillary pressure, p_0 the entry pressure and λ a dimensionless parameter. The values $k_{sat,ref} = 1.0 \cdot 10^{-19} \text{ m}^2$, $p_{0,ref} = 6.0 \cdot 10^5 \text{ Pa}$ and $\lambda = 0.24$ were obtained from permeability tests on BRIE cores, by fitting a retention curve for the rock matrix [Fransson et al., 2015] and are used here for the scaling relationship. On condition that they allow to build a model in line with tunnel inflows and pressures in the floor of the BRIE tunnel, we then adopt fixed distributed pressure values from the Äspö HRL flow model [Svensson et al., 2008] (see also supporting information S1) as boundary conditions to define the following inverse problem. Knowing the measured inflow into the BRIE tunnel at the intersection with wfrac1 and over the rest of the tunnel wall (two main targets), we aim to determine the saturated permeability values for three simplified equivalent materials: the background rock, the tunnel wall cells without fracture zone and the tunnel wall cells connected to wfrac1 or wfrac2 (one single value for both). The permeability of cells representing the fracture zones that are not directly in contact with the tunnel is uniform and fixed to the value estimated during hydraulic testing. As a

Table 1. Tunnel Inflow Targets

Inflow	Measured (mL/min)	Simulated (mL/min)	Relative Difference
wfrac1	78	76.2	-2.7%
diffuse	24	22.9	-4.4%

means for comparison, the validity of a stochastic continuum representation for background fractured rock has been discussed by *Finsterle* [2000] and it is considered applicable if the equivalent parameters can be calibrated with a data set acquired at a similar scale as the model and with a consistent set of processes at work. Although, the current approach with homogeneous permeabilities is simpler than

the stochastic continuum used by *Finsterle* [2000], we here hypothesize that it will be applicable under the same data and scale requirements.

The uncertainty introduced by the simplicity of the chosen conceptual model is likely to supersede any potential parametric uncertainty. For this reason, we proceed with a fitted set of permeability values (Table 3) such that these values honor tunnel inflows with a relative difference under 5% (Table 1) and the pressure values in the four 10 m-long boreholes drilled in the walls of the TASO tunnel with less than 15% difference (Figure 1a and Table 2). The discrepancy obtained for borehole K18B01 (Table 2) can be traced back to the imposed boundary condition and the parent Äspö flow model that indicates a liquid pressure value of $p_l = 11$ bar for that specific borehole location. For further comparison, one can observe that the selected background rock permeability value is close to the 3 m scale median permeability obtained across more than a thousand tested borehole intervals at the Äspö HRL as reported by *Vidstrand* [2003] (Table 3). Similarly, one can compare the selected tunnel wall permeability values in the absence of intersecting fracture zone to the median permeability reported by *Emsley et al.* [1997] for 1 m scale blocks tested at the tunnel wall. Finally the tunnel wall permeability value at the intersection with fracture zones is of the same order as the 95-percentile reported by *Emsley et al.* [1997], as could be expected for a locally very disturbed zone (Table 3). Based on these comparisons, the presented model of the BRIE tunnel including three fracture zones and three additional homogeneous material types was deemed fit to serve as a common framework in which to develop more detailed scenarios for realistic deposition hole characteristics.

3. Deposition Hole Scale Analyses

3.1. Development of Scenarios

Deposition hole scale models are developed for two main purposes. The first relates to main investigation question (1) of the study, namely testing the ability of numerical models to predict field-scale observations on de-saturation and re-saturation dynamics qualitatively and quantitatively. Hence, for the purpose of supporting model-experiment comparisons, model settings were adopted to honor field conditions as closely as possible. Two of the five original probing boreholes, tagged 17 and 18 during the BRIE experiments, were expanded to a diameter of 30 cm and a total depth of 3.5 m and 3 m respectively. The deposition hole scale model development then relied on the detailed characterization of these BRIE deposition holes. One parameter of interest is the open hole inflow rate. *Fransson et al.* [2015] reported inflow values of 0.12–0.25 mL/min for deposition hole 17 and 0.01–0.03 mL/min for deposition hole 18 (excluding the contribution of the tunnel EDZ that is estimated to penetrate between 0.5 and 1 m into the rock from the tunnel floor). One order of magnitude separates the inflow rates of the two deposition holes. In our basic model setup, we retained inflow rates of 0.18 mL/min and 0.018 mL/min as calibration targets for holes 17 and 18 respectively (Table 4, two last rows -DH17 and -DH18).

Another result of the characterization campaign is the actual vertical sections and fracture traces in each hole that contribute to the total inflow. For hole 17, the transmissivity of the hole section below the EDZ was estimated to $4.5 \cdot 10^{-11} \text{ m}^2/\text{s}$ by a long duration hydraulic flow test [*Fransson et al.*, 2015] and has been

Table 2. 10 m Borehole Long-Term Pressures

Borehole	Measured (bar)	Simulated (bar)	Relative Difference
K11A01	22.9	24.7	+7.7%
K11B01	3.2	3.6	+13.9%
K18A01	24.8	22.9	-7.6%
K18B01	21.0	12.6	-40.9%

mainly attributed to a flowing fracture intersecting the hole close to its bottom and likely indirectly connected to wfrac1 (Figure 1b). A vertical intersecting pegmatite vein was also discovered at the bottom of hole 17 and could have partly contributed to the total inflow, but this feature was neglected for the present study. For hole 18, there was no detectable inflow at first, but after hydraulic tests were performed at the BRIE site, a single

Table 3. Calibrated Rock Mass Permeabilities and Literature References

Permeability	Value	Reference Values	Source
background rock	$2.6 \cdot 10^{-17} \text{ m}^2$	$1.0 \cdot 10^{-17} \text{ m}^2$	median value reported by <i>Vidstrand</i> [2003]
tunnel skin w/o fracture	$1.2 \cdot 10^{-18} \text{ m}^2$	$5. \cdot 10^{-19} \text{ m}^2$	median value reported by <i>Emsley et al.</i> [1997]
tunnel skin w/fracture	$3.0 \cdot 10^{-17} \text{ m}^2$	$1.0 \cdot 10^{-17} \text{ m}^2$	95-percentile reported by <i>Emsley et al.</i> [1997]

fracture seems to have (re-)activated and to have been the main contributor to the aforementioned total inflow rate (Figure 1b).

To incorporate the available observational data from BRIE, we defined two different permeability structures that both honor identified fracture traces and total inflow rates (Table 4 columns FrL- and FrH-). These hypothetical and equally realistic permeability structures denoted “One fracture, low T_f ” (FrL-) and “One fracture, high T_f ” (FrH-) take in a fracture identified locally, meshed as a porous medium equivalent with a thickness of 1 cm and a constant local permeability k_m elsewhere. The difference between the simulation setups for FrL- and FrH- lies in the value adopted for the local matrix permeability. Scenarios FrL- consider the median rock matrix permeability estimation of $k_m = 10^{-20} \text{ m}^2$ obtained as a geometric average value in the laboratory tests on de-stressed vertical cores from the BRIE probing boreholes. The effective fracture transmissivities are then fitted in each case to respect the target total inflow rate into the open hole. Scenarios FrH- are representative of the lower laboratory values $k_m = 2. \cdot 10^{-21} \text{ m}^2$ obtained through permeability measurements performed on core samples in support to BRIE. The local fracture transmissivities are later fitted in each case to reach the prescribed inflow level. Interestingly, the calibrated transmissivity for FrH-DH17 is $2.35 \cdot 10^{-11} \text{ m}^2/\text{s}$, that is the same order of magnitude as the value estimated by field hydraulic tests, $4.5 \cdot 10^{-11} \text{ m}^2/\text{s}$ [*Fransson et al.*, 2015]. Comparison between cases FrL- and FrH- are useful in providing insight into how sensitive wetting can be expected to be with respect to contrasts between matrix flow and fracture flow.

In order to address main investigation question (2) regarding how prior inflow rates and inflow heterogeneity may influence the subsequent wetting of the buffer, we expand the BRIE-supported parameter combinations to an array of scenarios that would be more generally relevant for deposition hole characteristics in a KBS-3 type of repository. The first one denoted Homogeneous (Ho-) covers the possible case in which no single fracture contribution is dominant in the total inflow, and uses a constant local permeability value k_m for the rock mass located in a radius of 0.75 m from the hole axis. To make this scenario consistent with FrL- and FrH-, the local permeability k_m is estimated to fit the inflow rate targets previously defined (Table 4). A comparison between Ho- and FrL- will indicate to which extent a complete absence of focused fracture flow can influence wetting dynamics. Furthermore, considering the high end of the range of acceptable inflows based on the current design concept, we create a synthetic case (denoted -DH17*) in which the inflow rate of deposition hole 17 (having the highest inflow of the two BRIE holes) is further increased ten

Table 4. Table of Fitted Parameter Values With Corresponding Fracture and Matrix Inflows for All Deposition Hole Scale Scenarios

Permeability Distributionfixed Parameter Values → Target Inflow Rate ↓	Homogeneousprefix Ho- No fracture	One Fracture, Low T_f prefix FrL- $k_m = 1.0 \cdot 10^{-20} \text{ m}^2$	One Fracture, High T_f prefix FrH- $k_m = 2.0 \cdot 10^{-21} \text{ m}^2$
10 times measured inflow into deposition hole 17suffix -DH17* $Q \sim 3. \cdot 10^{-5} \text{ kg/s}$ $= 1.8 \text{ mL/min}$	calibrated parameter: $k_m = 1.3 \cdot 10^{-18} \text{ m}^2$ resulting inflows: Q_f : N/A $Q_m = 3.0 \cdot 10^{-5} \text{ kg/s}$	calibrated parameter: $T_f = 4.66 \cdot 10^{-11} \text{ m}^2/\text{s}$ resulting inflows: $Q_f = 3.0 \cdot 10^{-5} \text{ kg/s}$ $Q_m = 1.2 \cdot 10^{-8} \text{ kg/s}$	calibrated parameter: $T_f = 4.68 \cdot 10^{-11} \text{ m}^2/\text{s}$ resulting inflows: $Q_f = 3.0 \cdot 10^{-5} \text{ kg/s}$ $Q_m = 2.5 \cdot 10^{-9} \text{ kg/s}$
measured inflow into deposition hole 17suffix -DH17 $Q \sim 3. \cdot 10^{-6} \text{ kg/s}$ $= 0.18 \text{ mL/min}$	calibrated parameter: $k_m = 1.45 \cdot 10^{-19} \text{ m}^2$ resulting inflows: Q_f : N/A $Q_m = 3.0 \cdot 10^{-6} \text{ kg/s}$	calibrated parameter: $T_f = 4.1 \cdot 10^{-12} \text{ m}^2/\text{s}$ resulting inflows: $Q_f = 2.7 \cdot 10^{-6} \text{ kg/s}$ $Q_m = 2.0 \cdot 10^{-7} \text{ kg/s}$	calibrated parameter: $T_f = 2.35 \cdot 10^{-11} \text{ m}^2/\text{s}$ resulting inflows: $Q_f = 2.9 \cdot 10^{-6} \text{ kg/s}$ $Q_m = 3.0 \cdot 10^{-8} \text{ kg/s}$
measured inflow into deposition hole 18suffix -DH18 $Q \sim 3. \cdot 10^{-7} \text{ kg/s}$ $= 0.018 \text{ mL/min}$	calibrated parameter: $k_m = 1.8 \cdot 10^{-20} \text{ m}^2$ resulting inflows: Q_f : N/A $Q_m = 3.0 \cdot 10^{-7} \text{ kg/s}$	calibrated parameter: $T_f = 1.8 \cdot 10^{-13} \text{ m}^2/\text{s}$ resulting inflows: $Q_f = 1.4 \cdot 10^{-7} \text{ kg/s}$ $Q_m = 1.6 \cdot 10^{-7} \text{ kg/s}$	calibrated parameter: $T_f = 4.2 \cdot 10^{-13} \text{ m}^2/\text{s}$ resulting inflows: $Q_f = 2.7 \cdot 10^{-7} \text{ kg/s}$ $Q_m = 3.0 \cdot 10^{-8} \text{ kg/s}$

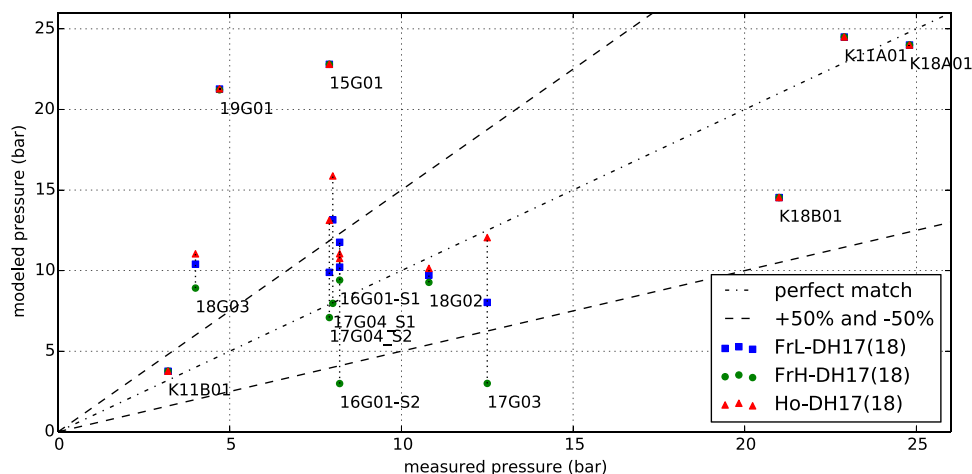


Figure 2. Long-term pressure in borehole intervals (see Figure 1b) surrounding the BRIE deposition holes, comparison between field measurements and modeled values according to different near field permeability structures.

times to an inflow rate of 1.8 mL/min (Table 4, first row -DH17*). Thereby, we will be able to analyze similarities and differences in wetting behaviors at significantly different inflow conditions, i.e., differing by up to two orders of magnitude.

The flow equations, outer and tunnel boundary conditions are kept from the previous tunnel scale calibration (section 2), since no air entrapment effects are expected for open deposition holes either. Additional atmospheric boundary conditions are implemented in the open deposition holes.

The long-term pressure field values measured in probing boreholes in the floor of the BRIE tunnel (Figure 1b) are compared against corresponding simulated pressures (Figure 2). This shows that the pressure values in the 10 m long boreholes in the BRIE tunnel wall K11A01, K11B01, K18A01 and K18B01 (Table 2) are not significantly affected by the mesh refinements operated at the two deposition hole locations, which shows the relevance of the selected background rock structure and parameters values at the tunnel scale. One can see that boreholes 16G01-S1 to 18G03 give reasonable pressure predictions (Figure 2). The inclusion of geometric information on the local fractures intersecting the deposition holes make scenarios FrL-DH17(18) and FrH-DH17(18) less prone to overestimate the pressure (Figure 2). The absence of fracture information and detailed inflow measurements further away from the deposition holes explains the larger mismatch between measured and modeled pressure (boreholes 15G01 and 19G01 in Figure 2).

3.2. Buffer Wetting: Model Assumptions and Experimental Data

After installation into the deposition hole, the bentonite buffer and the surrounding rock are under confined conditions, i.e., there is a risk for air entrapment due to the spatial heterogeneity of the water delivery, for example due to the presence/absence of conductive fractures or to internal variability of fracture properties (e.g., local aperture) and matrix properties (e.g., intrinsic permeability). To correctly represent confined conditions and possible air entrapment, it is necessary to include two coupled mass balances for air and water and to take into account the resorption of trapped air phase occurrences by air dissolution into the liquid phase. We assume that the partition of air between the gas and liquid phase is constantly at equilibrium following Henry's law and that the whole experiment happens under isothermal conditions. These assumptions are consistent with the TOUGH2 equation of state 3 (EOS3) [Pruess et al., 1999], which was used for the bentonite wetting simulations. Binary diffusion is incorporated using the Millington-Quirk model to parametrize tortuosity as implemented in TOUGH2 [Pruess et al., 1999]. The relative tolerance for convergence is relaxed 10^{-3} , in order to save computational time by matching the accuracy of the calculation with the large conceptual uncertainty introduced by the simple model adopted for the rock mass, following arguments presented by Nissen et al. [2015]. Cells with the highest residuals are usually located at the edge of the unsaturated zone in the rock wall.

The bentonite blocks are introduced as an equivalent porous medium for which we define customized unsaturated permeability laws as follows:

$$k_l = k_{sat} \cdot (S_l)^\alpha \quad (4)$$

$$k_g = k_{sat} \cdot \Gamma \cdot (1 - S_l)^\beta \quad (5)$$

$$p_{cap, confined} = -p_0 \cdot (S_l^{-1/\lambda} - 1)^{1-\lambda} \quad (6)$$

with k_l the liquid phase permeability, $k_{sat} = 6.4 \cdot 10^{-21} \text{ m}^2$ the water saturated permeability, k_g is the gas phase permeability, S_l the effective liquid phase saturation, $p_{cap, confined}$ the capillary pressure, $p_0 = 1.0 \cdot 10^7 \text{ Pa}$ the entry pressure, $\alpha = 4.$, $\beta = 2.$, $\Gamma = 10^4$ and $\lambda = 0.28$ dimensionless parameters. Values for α , λ and p_0 were adopted after laboratory water uptake tests for BRIE bentonite [Fransson et al., 2015]. Values for β and Γ were drawn from the literature for FEBEX bentonite [Alonso et al., 2005; Dessirier et al., 2015], but were shown to have little impact on times to reach saturation levels below 0.9. [Dessirier et al., 2015]. The swelling of the bentonite is implicitly accounted for in the retention curve by calibrating it against measurements made for similar confined configurations and according to a methodology developed by Dueck and Börgesson [2007]. For BRIE, the bentonite parcels had an initial bulk density of 1775 kg/m^3 (dry density of 1560 kg/m^3), an initial liquid saturation of 0.47 (corresponding to a relative humidity of 59%) and an initial capillary pressure of 70 MPa.

For unsaturated rock matrix or fractures, two gas permeability parametrizations were tested $k_{rg} = 1 - k_{rl}$ [Grant, 1977] and $k_{rg} = (1 - S_l^2)(1 - S_l)^2$ [Corey, 1954]. The second definition prescribes a reduction in the sum $k_{rl} + k_{rg}$ at intermediate levels of saturation, i.e., a mutual hindrance to flow for the two phases also known as phase interference effects. No significant difference could be observed between the two cases for early stages when the saturation levels essentially stay under 0.9, all subsequent results are thus presented only for the second formulation.

Six relative humidity sensors (Aitemin SHT75 V3) were put in place in each bentonite column, choosing in each case one section expected to be relatively wet and one section expected to be relatively dry. These sensors recorded relative humidity h of bentonite with continuous output in each hole during the wetting phase of BRIE with an estimated measurement error of the relative humidity units under 4%. The acquired relative humidity values were translated first to capillary pressure using Kelvin's equation [Edlefsen and Anderson, 1943]:

$$p_{cap} = \frac{\ln(h) \cdot \rho_w \cdot R \cdot T}{M_w} \quad (7)$$

where $\rho_w = 1000 \text{ kg/m}^3$ is the density of liquid water, $R = 8.314 \text{ J.K}^{-1}.\text{mol}^{-1}$ is the ideal gas constant, $T = 288.15 \text{ K}$ is the absolute temperature, $M_w = 1.8 \cdot 10^{-2} \text{ kg/mol}$ is the molecular weight of water. The obtained capillary pressure is then converted into liquid saturation by inverting the bentonite retention curve, equation (6). Because the retention curve for the bentonite blocks was established in the laboratory for blocks prepared identically to those installed in BRIE and showed very good reproducibility between different tests, the uncertainty involved in the conversion of the measurements from relative humidity to liquid saturation is assessed to be low.

The bentonite columns in holes 17 and 18 were dismantled and sampled out of the rock after 419 and 518 days respectively. Immediately after the retrieval of the bentonite columns, more than a thousand samples were taken from the lower 1.5 m in each column which is the section that was least influenced by the presence of the tunnel and its EDZ. The samples were analyzed for water content w and dry density ρ_d . These two measurements allowed to calculate the equivalent porosity Φ and liquid saturation S_l assuming a constant grain density $\rho_p = 2780 \text{ kg/m}^3$ and water density $\rho_w = 1000 \text{ kg/m}^3$ with the following relations:

$$\Phi = 1 - \frac{\rho_d}{\rho_p} \quad (8)$$

$$S_l = w \cdot \frac{\rho_p}{\rho_w} \cdot \frac{1 - \Phi}{\Phi} \quad (9)$$

Relative humidity measurements were also performed along four profiles of the dismantled deposition hole rock walls, three in hole 17 denoted as cross sections "Dry Section Upper" (DSU), "Dry Section Lower" (DSL) and "Fracture" (F) and one in hole 18 [Fransson et al., 2015] (Figure 3). Holes were drilled and lined with

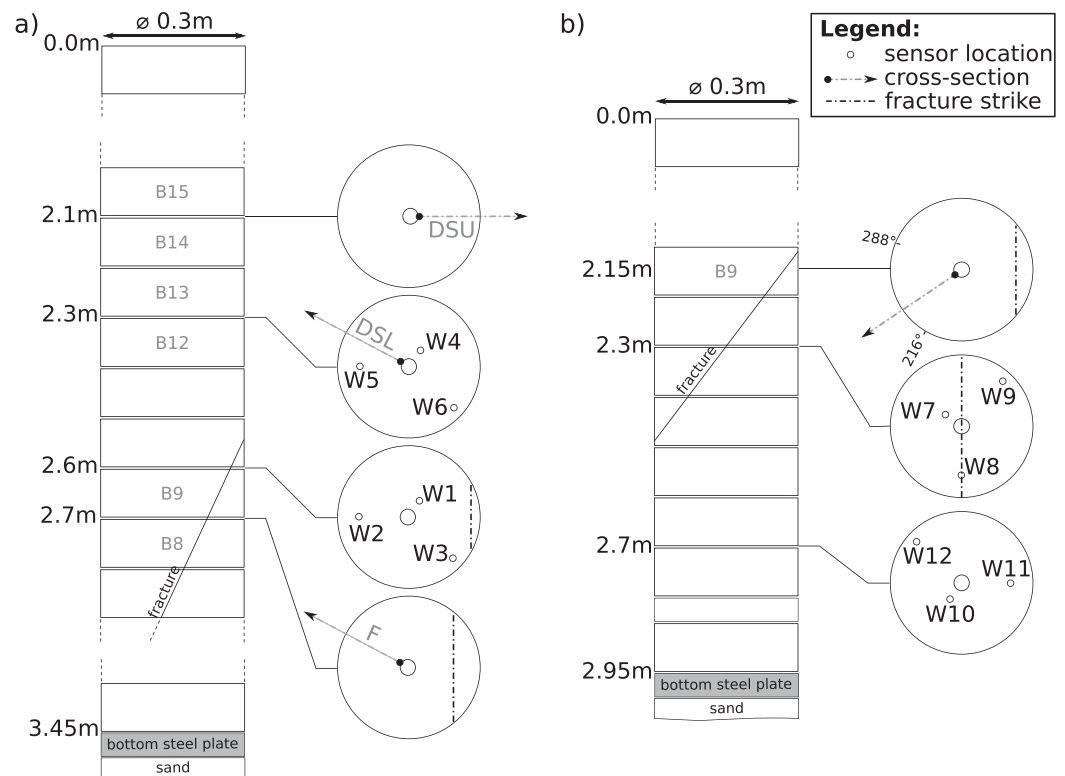


Figure 3. (a) Sensor positions and cross-section lines in hole 17: W1-6 and “Dry Section Upper” (DSU), “Dry Section Lower” (DSL) and close to “Fracture” (F). (b) Sensor positions and cross-section lines in hole 18: W7-12 and unnamed cross section.

plastic tubes in which the humidity sensors were inserted (Vaisala with a nominal measurement error of 2% relative humidity unit below 90% relative humidity and 3% above). By using equation (7) to get the capillary pressure p_{cap} and the scaled retention curve in equation (3) we converted the measured relative humidity into liquid saturation in the rock for comparison with the model outputs.

Finally, to compare the wetting rate from a global perspective and not only at specific sensor locations or cross sections, we present the cumulative density function (CDF) found for all the collected samples of liquid saturation in each of the two deposition holes at dismantling time. Then for each model, we compute the saturation CDF at every output time and we define the equivalent wetting time t_{eq} for each model as the time that minimizes the root mean square error between the modeled CDF and the experimental CDF at dismantling.

4. Predicted Buffer Wetting Under Different Scenarios

Liquid saturation over time obtained from the measured humidity values for the bentonite columns inserted in deposition hole 17 and 18 are shown in Figures 4 and 5 respectively (circle markers with error bars). Sensors W1-3 in hole 17 and W7-9 in hole 18 were positioned to capture sections of the holes that were expected to be directly influenced by an intersecting flowing fracture (Figures 3a and 3b) and thus wet. On the contrary, sensors W4-6 in hole 17 and W10-12 in hole 18 were placed to record the bentonite sections that were expected to have little access to groundwater and should thus remain relatively dry. However, an accidental flooding of the BRIE tunnel occurred approximately 37 days after the start of the experiment, leading to an increased access to water through the central tube used for the installation of the bentonite and the sensor wiring. The consequences of this event are visible in most sensor data series as elevated liquid saturation values shortly after test start (early peaks in Figures 4 and 5). The flooding is not included in the setup of the models, and these are not expected to reproduce any singular event up to 100 days after the start of the experiment, but rather to capture the trend of the measurement from approximately 100 days onward. For the above-mentioned drier sections with supposedly limited groundwater

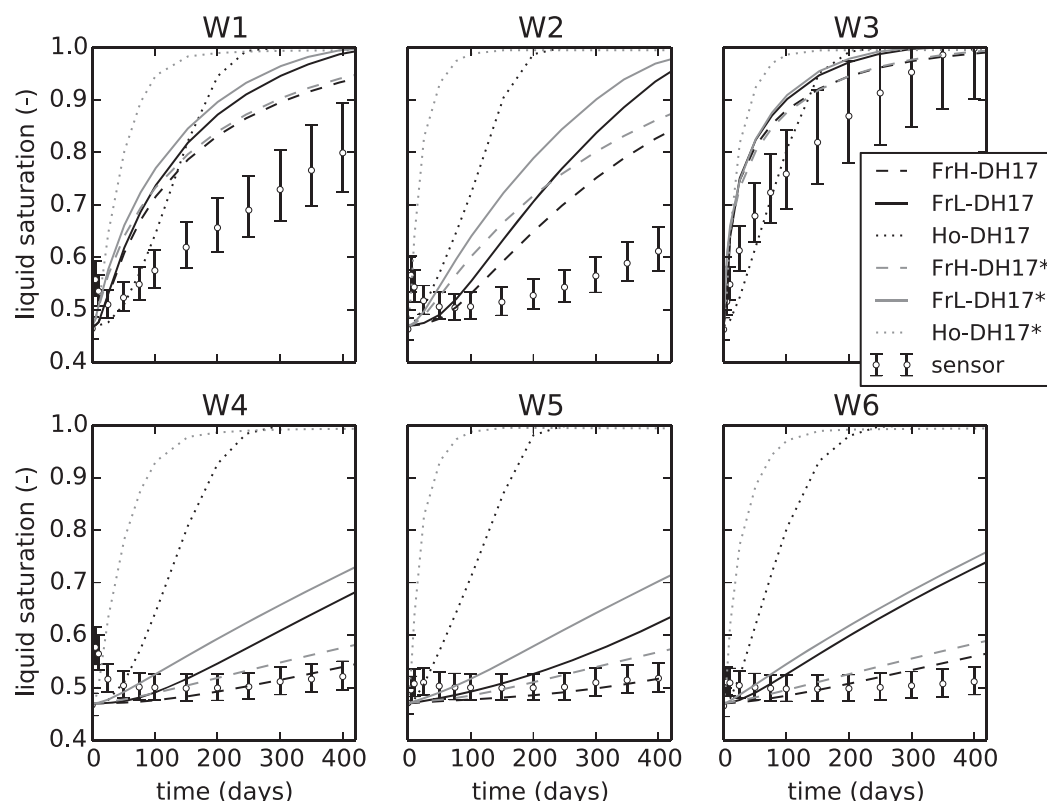


Figure 4. History of liquid saturation at sensor locations in hole 17 given the initial inflow measured in the field (black set of curves) and 10 times the initial inflow measured in the field (gray set of curves). Sensors W1-3 on the top row in this figure were located in an expected wet section close to the intersection with a mapped flowing fracture. W4-6 on the bottom row in this figure were located in a section surrounded by comparatively unfractured rock and thus expected to be dry.

access, water delivery through the central tube to the sand filter under the bottom plate may, in addition to possible action of uncharted fractures or rock matrix variability, explain the relatively more pronounced wetting in hole 18 (sensors W10-12, Figure 5 versus sensors W4-6, Figure 4).

The modeled wetting of the bentonite buffer following its installation is shown in Figure 4 for the six different sensor locations (W1–W6) and the six considered permeability distribution-inflow rate scenarios of deposition hole 17 (FrH-DH17, FrL-DH17, Ho-DH17, FrH-DH17*, FrL-DH17*, Ho-DH17*; Table 4). The corresponding results for the six sensor locations (W7–W12) and three considered scenarios (FrH-18, FrL-18, and Ho-18) of deposition hole 18 are shown in Figure 5. With few exceptions, homogeneous inflow conditions (Ho-; dotted lines) are predicted to yield much more rapid buffer wetting than configurations with an explicit fracture (FrL-; solid lines and FrH-; dashed lines). The differences are more pronounced for the hole 17 scenarios that have higher total inflows and higher contrasts between the fracture and the matrix flow rates than the hole 18 scenarios. In contrast, a comparison between the three scenarios that had an initial total inflow Q of 0.18 mL/min (Figure 4, black lines denoted as -DH17) with the three scenarios that had an initial inflow that was ten times larger (Figure 4; gray lines denoted as -DH17*) show only small differences in the wetting times in most cases. The exceptions consist of the homogeneous cases (dotted lines in Figure 4). Nevertheless, the predicted homogeneous case differences (related to the order of magnitude difference in initial inflow or water supply to the buffer), are still smaller than the predicted differences in wetting times caused by introducing heterogeneity in the inflow distributions (Ho-, FrL- and FrH-; Figure 4). Generic cases with a homogenized rock mass description and thus a higher equivalent permeability by *Gens et al.* [2002] also showed a rapid re-saturation of the rock and subsequent hydration of the buffer. *Gens et al.* [2002] invited for caution regarding the interpretation and representativity of results from models with homogenized equivalent properties. A possible explanation for the buffer wetting being relatively insensitive to the initial supply of water from the adjacent rock is that the wetting is limited by properties of the bentonite, and/or the zone around the bentonite-rock interface. It is plausible that such a limitation would be more

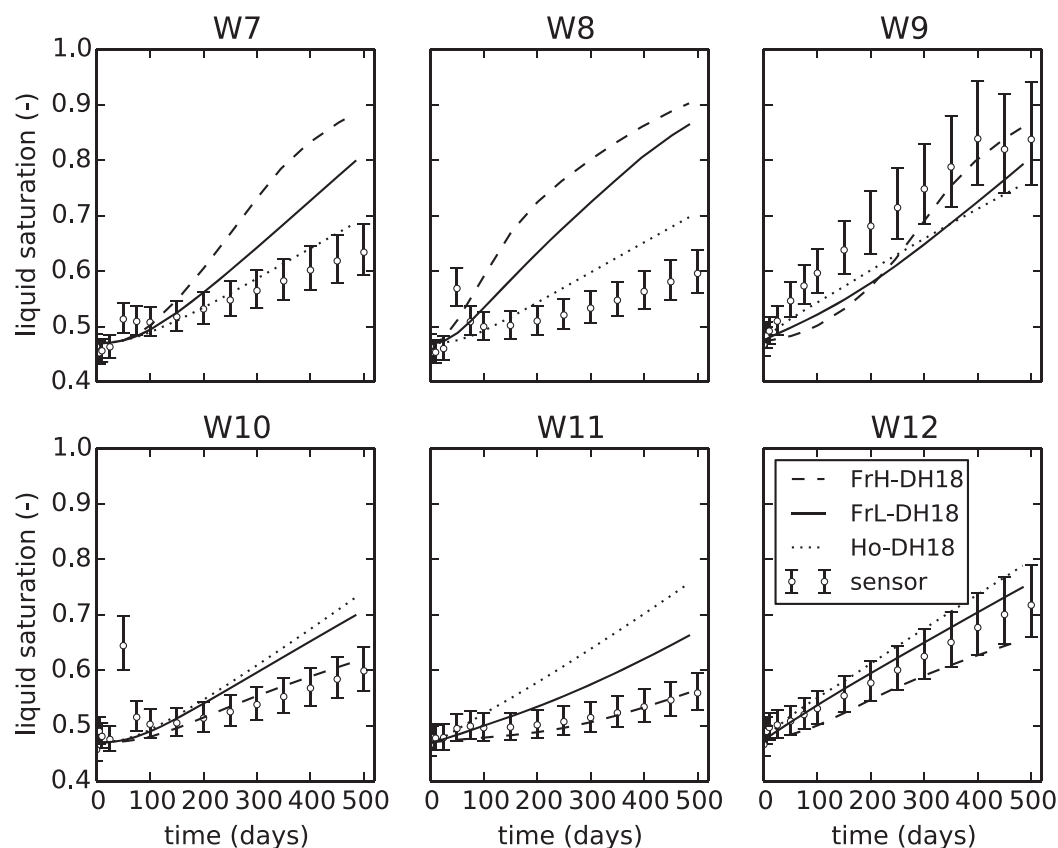


Figure 5. History of liquid saturation at sensor locations in hole 18. W7-9 on the top row in this figure were facing the trace of a mapped flowing fracture, and thus expected to be in a wet section. W10-12 on the bottom row in this figure were located in an unfractured section according to the prior rock characterization, and thus expected to be dry.

effective for channelized flow, i.e., the heterogeneous cases in Figure 4, explaining why they are more insensitive to initial inflow Q than the homogeneous cases.

Comparing the wetting results from the model representations that honored the actual deposition hole characteristics of BRIE (scenarios FrH-DH17 and FrL-DH17 of Figure 4 and scenarios FrH-DH18 and FrL-DH18 of Figure 5) with the observed sensor data from BRIE (circles in Figures 4 and 5), one can see that the models generally capture the relative differences in wetting rates between the different cases, e.g., being able to predict in which setting and location wetting would be the fastest. However, in absolute terms, most models show an overestimation of the bentonite wetting rates as can be evidenced by sensor histories (Figures 4 and 5) and final saturation profiles along cross sections (Figure 6). In the case of hole 17, it can be observed that reducing the matrix intrinsic permeability (FrH-DH17 versus FrL-DH17) consistently improved the prediction at all sensor locations (Figure 4) and brought a significant improvement in the final profiles in the dry bentonite sections (Figures 6a and 6b). More generally, the overestimation is highest near the flowing fracture traces (Figures 4 and 5), indicating that some inflow reduction effect and/or in-fracture variability constrain the water delivery at the rock bentonite interface but are not represented by the chosen parametrization. Possible effects include hysteresis behavior in the rock mass that undergoes a cycle of desaturation/re-saturation, stress-redistribution impacting the fracture transmissivity, intrinsic variability in permeability or combinations of these. Regarding hysteresis, it is worth pointing out that the adopted constitutive relationships for bentonite were fitted on laboratory results acquired under an imbibition regime, which is consistent with the situation observed in the field. The situation is more complicated for the rock wall that undergoes drainage first and then imbibition. The nonhysteretic tentative constitutive relationships adopted for rock were compiled from a data set comprising both imbibition and drainage experiments. Accounting for hysteresis by shifting the retention curve toward lower magnitudes (e.g., with a higher exponent λ) during imbibition or by accounting for the development of a residual gas saturation

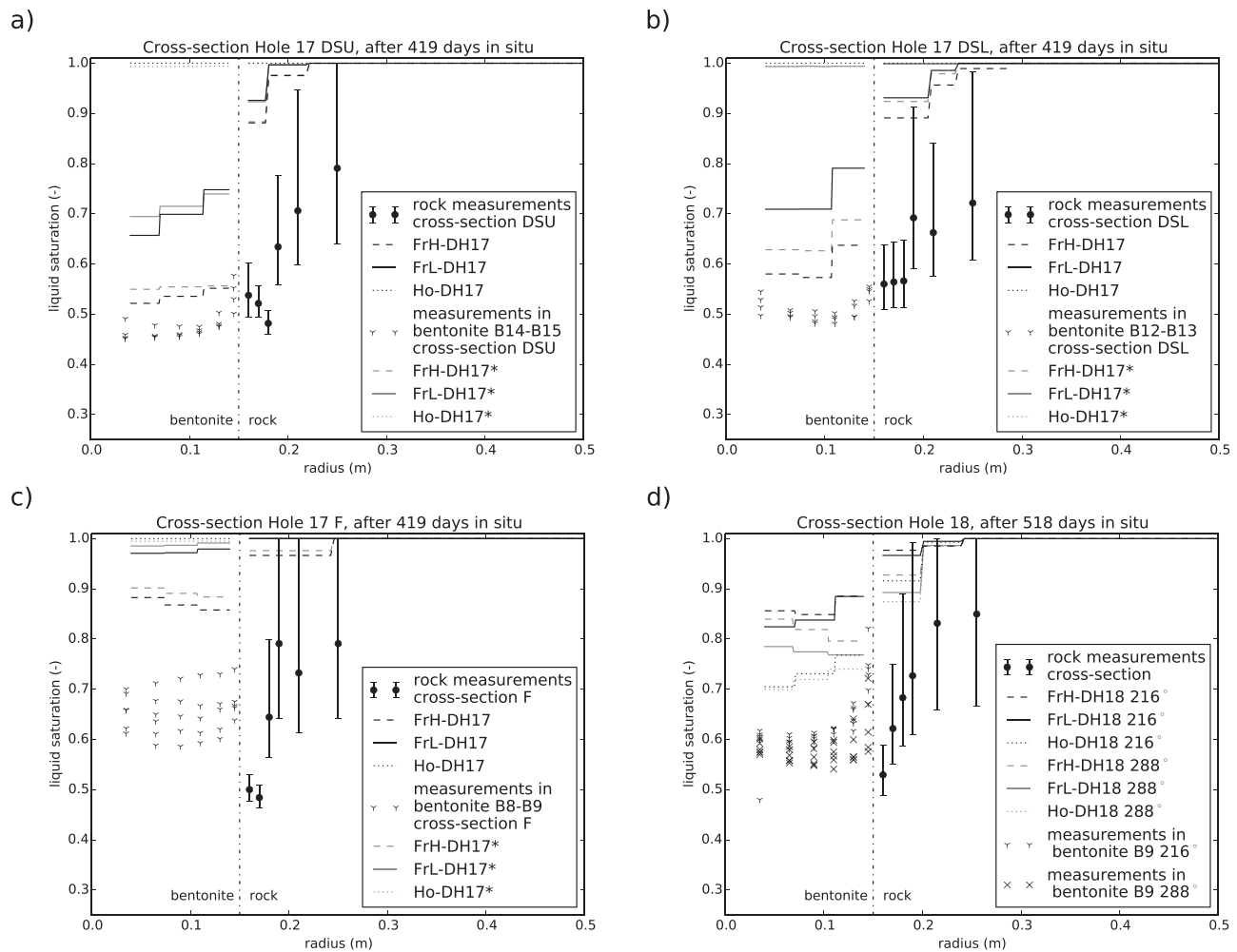


Figure 6. Final liquid saturation profile along cross-section (a) “Dry Section Upper”-DSU, (b) “Dry Section Lower”-DSL and (c) close to “Fracture”-F in deposition hole 17 (Figure 3a) and (d) the unnamed cross-section in deposition hole 18 (Figure 3b) according to data and the different scenarios, after 419 days in hole 17 and 518 days in hole 18 respectively. It should be noted that the directions of the humidity profile in the rock wall and of the bentonite sampling in hole 18 did not match exactly, the figure shows the two closest directions available for bentonite samples and for model outputs 216° (data shown by “Y” symbols and models in black) and 288° (data shown by “X” symbols and models in gray).

(bubble trapping) could both account for significantly lower saturations in the rock for longer periods of time.

Figure 6 compares the field measurements in both bentonite and rock to the different model results along the cross section lines depicted in Figure 3. It should be noted that the directions of the humidity profile in the rock wall and of the bentonite sampling in hole 18 did not match exactly, which is why Figure 6d shows the two closest directions available for bentonite samples and for model outputs 216° (data shown by “Y” symbols and models in black) and 288° (data shown by “X” symbols and models in gray). The experimental results obtained in BRIE (crosses in Figure 6) show substantial de-saturation of the rock around the deposition hole at the end of the experiment after ~500 days, which is of the same order as an estimated median time of around 400 days needed to re-saturate the rock [Dessirier et al., 2015], based on a large set of generic simulations of BRIE-size deposition holes. Dessirier et al. [2015] concluded that a correct understanding and parametrization of two-phase flow in the rock and in bentonite, including air dissolution and diffusion into the liquid phase, was crucial to estimate the residence time of air in the system. The occurrences of sustained de-saturation in the deepest parts of the BRIE deposition holes hence provide observation-based evidence of the conclusion obtained through modeling and global sensitivity analysis by Dessirier et al. [2015].

Similar conclusions can be drawn by considering the induced difference by the same scenarios on the equivalent time to match the saturation distribution of the real system (Figure 7). This would indicate that

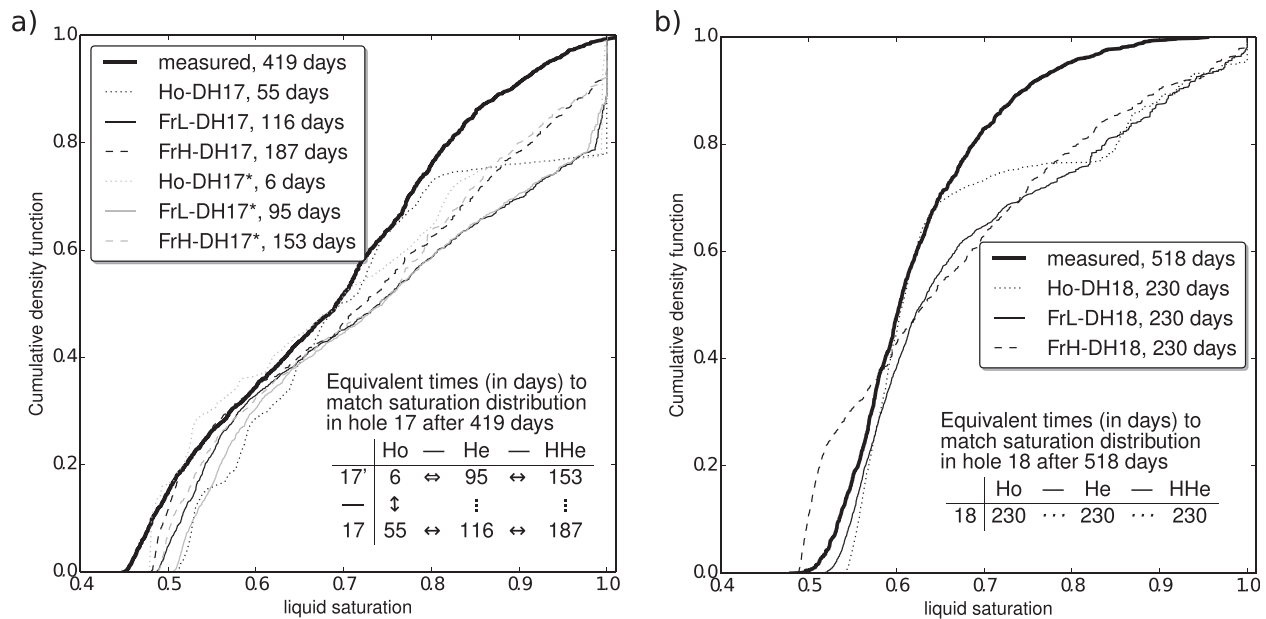


Figure 7. Cumulative distribution of liquid saturation in bentonite measured (a) in deposition hole 17 after 419 days and (b) in deposition hole 18 after 518 days together with the closest distribution (minimal least-square error) for each corresponding modeling scenario to determine the equivalent wetting time. Arrow thicknesses in the tables indicate the magnitude of change between scenarios.

the mere deposition hole inflow before buffer installation is a poor predictor of the subsequent wetting rate of the buffer for deposition holes that are highly dominated by sparse fracture inflows. The nearby matrix permeability structure becomes an important factor as it controls the spreading of the influence of the fracture away from the fracture plane and direct intersection with the deposition hole.

5. Conclusions

Two-phase flow simulations of an in-situ field experiments (BRIE) in which a bentonite buffer was inserted in small-scale deposition holes in a tunnel section of the Äspö Hard Rock Laboratory (Sweden) were carried out using TOUGH2. An array of modeling scenarios was designed to assess our capacity to reproduce the unsaturated flow dynamics in the installed buffer and in the deposition rock wall. Based on the numerical results and the comparison with field data, the main conclusions drawn from the stated investigation questions are summarized as follows.

BRIE provided experimentally based support for the fact that an unsaturated zone can develop beyond the deposition hole wall in a low permeable crystalline rock matrix. The numerical simulations could capture this de-saturation to a certain degree; the results indicated a thinner de-saturated layer around the deposition hole and that prevailed for shorter times than shown by the field evidence. These differences could be the result of model simplifications regarding the structure of the rock wall (e.g., homogeneous local rock matrix, few fractures considered, no fracture variability/flow channeling). Homogenized models, either fully or with a few local homogeneous fracture planes intersecting the deposition holes, showed a tendency to overestimate the wetting rates of the buffer thereby resulting in underestimating wetting times. Other, unaccounted two-phase or coupled processes could also lead to a slower wetting and should also be investigated, e.g., hysteresis behavior in the rock mass that undergoes a cycle of de-saturation/re-saturation and may develop a gas residual saturation (bubble trapping) or stress-redistribution impacting the fracture transmissivity/channeling.

A comparison between modeling scenarios gave new insights regarding the use of deposition hole characterization data for predicting wetting rates of bentonite. It was found that the total inflow rate into the deposition hole before it is backfilled with the bentonite buffer is a poor predictor of the future wetting rate of the buffer for cases where the inflow is dominated by a few fractures with moderate to high inflow rates. Instead, for such cases it is found that the location of the fracture intersection with the deposition hole as

well as the permeability of the local adjacent rock mass are more important factors to enable correct wetting predictions. Homogeneous model structures fitted to the open-hole measured inflow value, i.e., without any representation of the fractures intersecting the deposition hole, generally yield much more rapid buffer wetting than cases with representations of fractures intersecting the deposition hole, and are thus shown to be unfit for the assessment of buffer wetting time.

Acknowledgments

This work was partly funded by the Swedish Nuclear Fuel and Waste Management Company (SKB). The authors are grateful to the organizers and participants of the SKB Task Force for Modeling of Groundwater Flow and Transport of Solutes, within which the BRIE experiments were conducted. In particular, experimental setups developed and data on bentonite provided by Mattias Åkesson and colleagues at Clay technology were of great importance to this work. We also thank the staff at the Äspö HRL for their invaluable help in making the BRIE experiment possible. All data for this paper are either presented in the tables and figures or properly cited and referred to in the reference list. Three anonymous reviewers are also acknowledged for their constructive comments that helped to improve the manuscript.

References

- Alonso, E. E., et al. (2005), The febex benchmark test: Case definition and comparison of modelling approaches, *Int. J. Rock Mech. Min. Sci.*, 42(5), 611–638.
- Blessent, D., R. Therrien, and C. W. Gable (2011), Large-scale numerical simulation of groundwater flow and solute transport in discretely fractured crystalline bedrock, *Adv. Water Resour.*, 34(12), 1539–1552.
- Corey, A. T. (1954), The interrelation between gas and oil relative permeabilities, *Prod. Mon.*, 19(1), 38–41.
- Croucher, A. (2011), Pytough: A python scripting library for automating tough2 simulations, in *proceedings of 2011 New Zealand Geothermal Workshop held at University of Auckland's Faculty of Engineering*, pp. 21–23, Auckland, New Zealand.
- Cvetkovic, V., and A. Frampton (2010), Transport and retention from single to multiple fractures in crystalline rock at Äspö (Sweden): 2. fracture network simulations and generic retention model, *Water Resour. Res.*, 46, W05506, doi:10.1029/2009WR008030.
- Cvetkovic, V., and A. Frampton (2012), Solute transport and retention in three-dimensional fracture networks, *Water Resour. Res.*, 48, W02509, doi:10.1029/2011WR011086.
- Cvetkovic, V., J. Selroos, and H. Cheng (1999), Transport of reactive tracers in rock fractures, *J. Fluid Mech.*, 378(335–356).
- Cvetkovic, V., S. Painter, N. Outters, and J. Selroos (2004), Stochastic simulation of radionuclide migration in discretely fractured rock near the Äspö hard rock laboratory, *Water Resour. Res.*, 40, W02404, doi:10.1029/2003WR002655.
- Dessirier, B., J. Jarsjö, and A. Frampton (2014), Modeling two-phase-flow interactions across a bentonite clay and fractured rock interface, *Nucl. Technol.*, 187(2), 147–157.
- Dessirier, B., A. Frampton, and J. Jarsjö (2015), A global sensitivity analysis of two-phase flow between fractured crystalline rock and bentonite with application to spent nuclear fuel disposal, *J. Contam. Hydrol.*, 182, 25–35.
- Dueck, A., and L. Börgesson (2007), Model suggested for an important part of the hydro-mechanical behaviour of a water unsaturated bentonite, *Eng. Geol.*, 92(3), 160–169.
- Dverstorp, B., J. Andersson, and W. Nordqvist (1992), Discrete fracture network interpretation of field tracer migration in sparsely fractured rock, *Water Resour. Res.*, 28(9), 2327–2343.
- Edlefsen, N. E., and A. B. C. Anderson (1943), Thermodynamics of soil moisture, *Hilgardia*, 5(2), 31–298.
- Emsley, S., O. Olsson, L. Stenberg, H. Alheid, and S. Falls (1997), ZEDEx—A study of damage and disturbance from tunnel excavation by blasting and tunnel boring, technical report number TR 97-30, Swedish Nuclear Fuel and Waste Manage. Co., Stockholm. [Available at www.skb.se/publications.]
- Finsterle, S. (2000), Using the continuum approach to model unsaturated flow in fractured rock, *Water Resour. Res.*, 36(8), 2055–2066.
- Finsterle, S., and K. Pruess (1995), Solving the estimation-identification problem in two-phase flow modeling, *Water Resour. Res.*, 31(4), 913–924.
- Fiori, A., F. Boso, F. P. de Barros, S. De Bartolo, A. Frampton, G. Severino, S. Suweis, and G. Dagan (2010), An indirect assessment on the impact of connectivity of conductivity classes upon longitudinal asymptotic macrodispersivity, *Water Resour. Res.*, 46, W08601, doi:10.1029/2009WR008590.
- Follin, S., L. Hartley, S. Joyce and N. Marsic (2008), Regional hydrogeological modelling for Forsmark stage 2.3: Conceptual model development and numerical modelling using CONNECTFLOW, *Tech. Rep. SKB R-08-23*, Swed. Nucl. Fuel and Waste Manage. Co., Stockholm. [Available at www.skb.se/publications.]
- Frampton, A., and V. Cvetkovic (2010), Inference of field-scale fracture transmissivities in crystalline rock using flow log measurements, *Water Resour. Res.*, 46, W11502, doi:10.1029/2009WR008367.
- Frampton, A., and V. Cvetkovic (2011), Numerical and analytical modeling of advective travel times in realistic three-dimensional fracture networks, *Water Resour. Res.*, 47, W02506, doi:10.1029/2010WR009290.
- Fransson, Å., J. Thörn, L. Ericsson, M. Lönnqvist, and M. Stigsson (2012), Hydromechanical characterization of fractures close to a tunnel opening: A case study, paper presented at ISRM International Symposium-EUROCK 2012, Int. Soc. for Rock Mech., pp. 28–30, Stockholm, Sweden.
- Fransson, Å., M. Åkesson, and L. Andersson (2015), Bentonite Rock Interaction Experiment characterization of rock and installation, hydration and dismantling of bentonite parcels, technical report number R-14-11, Swed. Nucl. Fuel and Waste Manage. Co., Stockholm. [Available at www.skb.se/publications.]
- Gens, A., L. d. N. Guimaraes, A. Garcia-Molina, and E. Alonso (2002), Factors controlling rock–clay buffer interaction in a radioactive waste repository, *Eng. Geol.*, 64(2), 297–308.
- Grant, M. A. (1977), Permeability reduction factors at Wairakei, *Mech. Eng.*, 99(10), 105–105.
- Holton, D., S. Baxter, and A. Hoch (2012), Modelling coupled processes in bentonite: Recent results from the UK's contribution to the Äspö EBS Task Force, *Mineral. Mag.*, 76(8), 3033–3043.
- Huseby, O., J.-F. Thovert, and P. Adler (2001), Dispersion in three-dimensional fracture networks, *Phys. Fluids*, 13(3), 594–615.
- Hyman, J. D., C. W. Gable, S. L. Painter, and N. Makedonska (2014), Conforming delaunay triangulation of stochastically generated three dimensional discrete fracture networks: A feature rejection algorithm for meshing strategy, *SIAM J. Sci. Comput.*, 36(4), A1871–A1894.
- Jarsjö, J., and G. Destouni (2000), Degassing of deep groundwater in fractured rock around boreholes and drifts, *Water Resour. Res.*, 36(9), 2477–2492.
- Johannesson, L., L. Börgesson, R. Goudarzi, T. Sandén, D. Gunnarsson, and C. Svemar (2007), Prototype repository: A full scale experiment at Äspö HRL, *Phys. Chem. Earth, Parts A/B/C*, 32(1), 58–76.
- Krauskopf, K. (1988), *Radioactive Waste Disposal and Geology*, vol. 1, Springer Sci. & Bus. Media.
- Leverett, M. (1941), Capillary behavior in porous solids, *Trans. AIME*, 142(01), 152–169.
- Moreno, L., and I. Neretnieks (1993), Flow and nuclide transport in fractured media: The importance of the flow-wetted surface for radionuclide migration, *J. Contam. Hydrol.*, 13(1–4), 49–71.
- National Research Council (1996), *Rock Fractures and Fluid Flow: Contemporary Understanding and Applications*, Natl. Acad. Press, Washington, D. C.

- Neretnieks, I. (1980), Diffusion in the rock matrix: An important factor in radionuclide retardation?, *J. Geophys. Res.*, 85(B8), 4379–4397.
- Neuman, S. P. (2005), Trends, prospects and challenges in quantifying flow and transport through fractured rocks, *Hydrogeol. J.*, 13(1), 124–147.
- Niemi, A., K. Kontio, A. Kuusela-Lahtinen, and A. Poteri (2000), Hydraulic characterization and upscaling of fracture networks based on multiple-scale well test data, *Water Resour. Res.*, 36(12), 3481–3497.
- Nissen, A., P. Pettersson, E. Keilegavlen, and J. Nordbotten. (2015), Incorporating geological uncertainty in error control for linear solvers, paper presented at SPE Reservoir Simulation Symposium, Soc. of Pet. Eng., pp. 23–25, Houston, Tex.
- Pruess, K., G. Moridis, and C. Oldenburg (1999), *TOUGH2 User's Guide, Version 2.0*, Lawrence Berkeley Natl. Lab., Berkeley, Calif.
- Pusch, R. (2009), *Geological Storage of Highly Radioactive Waste: Current Concepts and Plans for Radioactive Waste Disposal*, Springer Sci. & Bus. Media. Springer-Verlag, Berlin, Heidelberg.
- Rycroft, C. (2009), Voronoi++: A three-dimensional voronoi cell library in c++, *Chaos*, 041111 pp.
- Sandén, T., and L. Börgesson (2010), Early effects of water inflow into a deposition hole, *Tech. Rep. SKB R-10-70*, Svensk Kärnbränslehantering AB, Stockholm, Sweden.
- Selroos, J.-O., and S. L. Painter (2012), Effect of transport-pathway simplifications on projected releases of radionuclides from a nuclear waste repository (sweden), *Hydrogeol. J.*, 20(8), 1467–1481.
- SKB (2010), Design and production of the kbs-3 repository (TR-10-12), report number is TR-10-12, Swedish Nuclear Fuel and Waste management Company (SKB), Stockholm. [Available at www.skb.se/publications.]
- Svensson, U., P. Vidstrand, I. Neretnieks, and B. Wallin (2008), Towards a new generation of flow and transport models for the Äspö Hard Rock Laboratory, main results from the project Äspö models 2005, technical report number R-08-74, Swed. Nucl. Fuel and Waste Manage. Co., Stockholm. [Available at www.skb.se/publications.]
- Van Genuchten, M. T. (1980), A closed-form equation for predicting the hydraulic conductivity of unsaturated soils, *Soil Sci. Soc. Am. J.*, 44(5), 892–898.
- Vidstrand, P. (2003), Äspö Hard Rock Laboratory, update of the hydrogeological model 2002, technical report number IPR-03-35, Swed. Nucl. Fuel and Waste Manage. Co., Stockholm. [Available at www.skb.se/publications.]